

# Vibration Attenuation Approach for Spaceborne Optical Interferometers

Gregory W. Neat  
neat@hucy.jpl.nasa.gov  
(818) 354-0584

James W. Melody  
jmelody@csi.jpl.nasa.gov  
(818) 354-0615

Boris J. Lurie  
B.J.Lurie@jpl.nasa.gov  
(818) 354-3690

Jet Propulsion Laboratory,  
California Institute of Technology  
4800 Oak Grove Drive  
Pasadena, CA 91109

November 11, 1997

## Abstract

This paper proposes a vibration attenuation strategy for spaceborne optical interferometers to meet their sub-micron positional stability requirements. Specifically, the Stellar Interferometer Mission requires 10-nanometer level stabilization of optical elements distributed across a 10 m flexible structure in the presence of the primary disturbance source, spinning reaction wheel assemblies. The proposed strategy incorporates the high-frequency attenuation of six-axis vibration isolation with low-frequency attenuation of active optical control. The strategy is implemented on the Micro-Precision Interferometer testbed, a fully-functional hardware model of a future spaceborne interferometer. Combining measured testbed disturbance transfer functions with a stochastic model of reaction wheel disturbances enables evaluation of the vibration attenuation strategy in the expected on-orbit disturbance environment. Results indicate that the requirement of 10 nm is satisfied.

## 1 Introduction

Optical interferometers use an array of two or more smaller telescopes, as opposed to a single large telescope, to collect light from a single target star. The light from these telescopes, or sub-apertures, is combined to create an interference fringe pattern. By measuring the fringe pattern for different interferometer orientations relative to the target star, an aperture with diameter equal to the largest separation of sub-apertures (the interferometer baseline) is synthesized.

The Stellar Interferometer Mission (SIM) is a first-generation spaceborne interferometer with astrometric and imaging goals [1]. Unlike ground-based interferometers bolted to

bedrock [2, 3], instrument optics of SIM are distributed across a 10 m, light-weight structure. The primary mechanical disturbance sources exciting the structure are expected to be the spinning reaction wheels used as actuators for the attitude control system. Simulation results suggest that in the unattenuated spacecraft environment, the fringe position variation is a factor of one hundred above the 10 nm requirement [4].

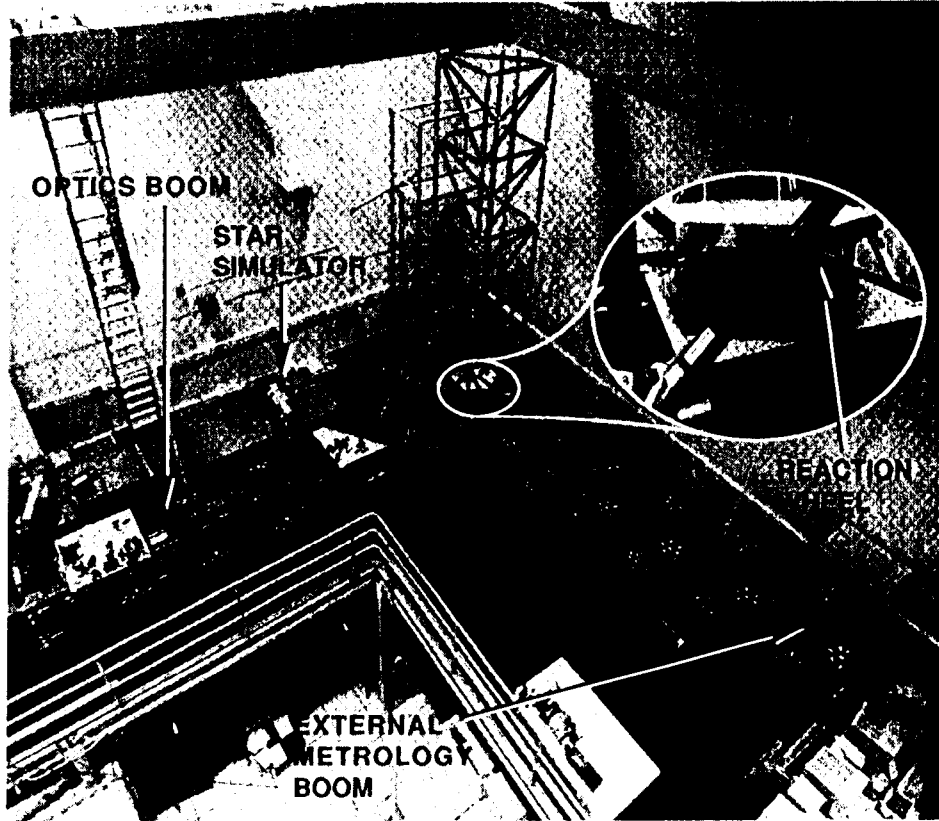


Figure 1: Bird's eye view of the MPI testbed with inset showing a close-up of the six-axis isolation system.

Reference [5] presents a layered vibration attenuation concept of disturbance isolation, structural quieting, and optical control. This approach was evaluated on a 3 m cantilevered truss structure containing a subset of interferometer optical elements and a uni-directional shaker. In this paper, a similar approach is applied to the Micro-Precision Interferometer (MPI) testbed, a full-size suspended hardware model of a stellar interferometer containing the complete set of optical components and a six degree of freedom disturbance source.

Figure 1 shows a bird's eye view of the MPI testbed. Located at the Jet Propulsion Laboratory, the MPI testbed contains all the subsystems necessary to assess the vibration attenuation technology effectiveness. These subsystems are: a 7 m x 7 m x 6.5 m softly suspended truss structure with mounting plates for subsystem hardware; a six-axis vibration isolation system which can support a reaction wheel assembly to provide a flight-like input disturbance source; a complete Michelson interferometer; internal and external metrology

systems; and a star simulator that provides stellar input to the interferometer collecting apertures.

The primary objective of the testbed is to realistically capture the on-orbit disturbance problem, in order to evaluate viable vibration attenuation strategies. This paper describes the expected disturbance source and its characterization, the specific vibration attenuation strategy, its control system implementation, and the prediction of on-orbit instrument performance using this strategy.

## 2 Disturbance Description

The SIM design baselines Hubble Space Telescope (HST) reaction wheels primarily because they are the quietest wheels flown to date. The mechanical vibrations (forces and torques) of these reaction wheels were measured and subsequently modeled as harmonics of the wheel speed [6]. For SIM, the wheel speed during observations will vary as the spacecraft attitude control system reacts to external torques. Furthermore, if the wheels are biased at different speeds, momentum will be transferred between wheels during a slew. Any useful disturbance model must account for this variability while providing a characterization amenable to disturbance analysis and control system disturbance-rejection design.

Since external torques are expected to be small for SIM, variation in wheel speed during a given observation is negligible, and the wheel speeds can be assumed constant over any given observation period. However, variation of wheel speeds between observations due to slewing and the action of external torques over time cannot be neglected. A comprehensive disturbance analysis must account for this variation between observations. This study uses a stochastic characterization of the wheel speed variations from one observation to the next. This representation considers the wheel speed as a random variable, justified by the assumption of constancy over each observation. The result is broadband disturbance power spectral densities that are useful for design of linear, time-invariant vibration attenuation strategies accommodating all possible wheel speeds.

Based on test data obtained from the HST flight units [6], the disturbance forces and torques are modeled as discrete harmonics of the reaction wheel speed,  $f_{rwa}$ , with amplitudes proportional to the wheel speed squared:

$$m(t) = \sum_{i=1}^n C_i f_{rwa}^2 \sin(2\pi h_i f_{rwa} t + \phi_i) \quad (1)$$

where  $m(t)$  is the disturbance torque or force,  $C_i$  is an amplitude coefficient,  $h_i$  is the harmonic number, and  $\phi_i$  is a random phase (uniform over  $[0, 2\pi]$ ) used to account for phase uncertainty. According to this model,  $h_i$  and  $C_i$  uniquely determine the amplitude and frequency of each harmonic component for a given wheel speed.

The disturbances modeled are one axial force (along the wheel spin axis), two radial forces (normal to the spin axis), and two radial torques (causing wheel wobble). These disturbances result from wheel imbalances and bearing imperfections [6]. Disturbance torque about the

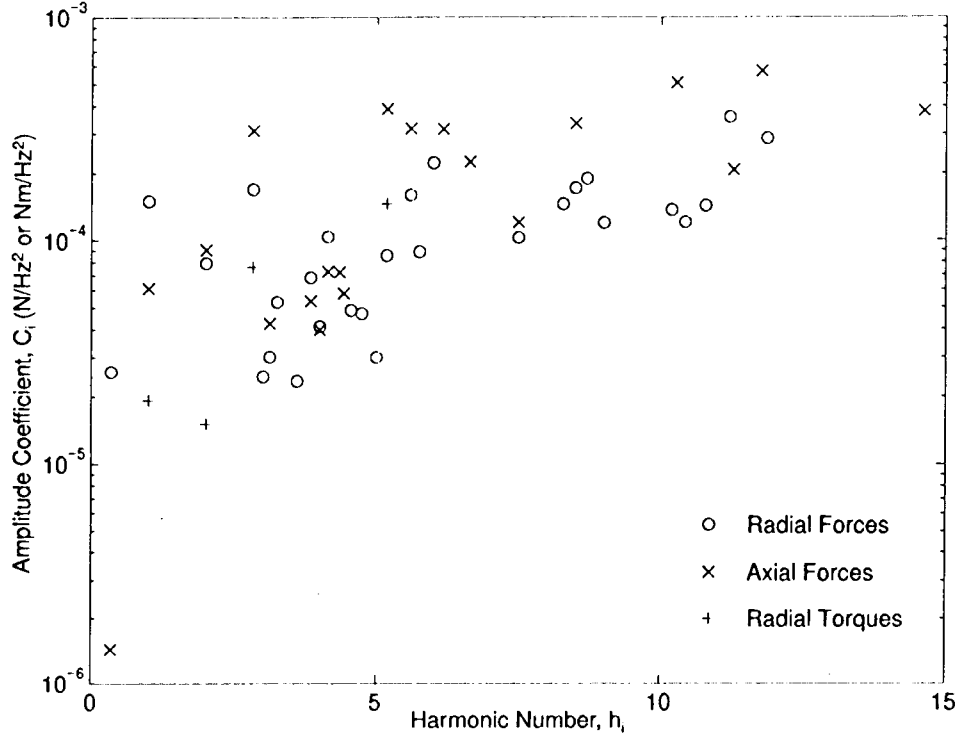


Figure 2: Plot of  $C_i$  versus  $h_i$  for each reaction wheel disturbance direction (see Eq. 1 for definitions). In general,  $h_i$  are not integers.

axis of rotation (torque ripple and motor cogging) was found to be insignificant. Figure 2 shows  $C_i$  plotted versus  $h_i$  for each of the disturbances.

The stochastic broadband model can be created from the discrete-frequency model of Eq. 1 by assuming that the wheel speed is a random variable with probability density function  $f_p(u)$ . In this case the autocorrelation of the disturbance,  $R_m(\tau)$ , is:

$$\begin{aligned} R_m(\tau) &= E \{m(t)m(t - \tau)\} \\ &= \sum_{i=1}^n \frac{C_i^2}{2} E \left\{ f_{rwa}^4 \cos(2\pi h_i f_{rwa} \tau) \right\} \end{aligned} \quad (2)$$

where  $E \{\bullet\}$  is the expected value operator [7]. The Fourier transform of  $R_m(\tau)$  is the power spectral density,  $\Phi_m(\omega)$ :

$$\Phi_m(\omega) = \sum_{i=1}^n \frac{\pi C_i^2 \omega^4}{2(2\pi h_i)^5} \left[ f_p \left( \frac{\omega}{2\pi h_i} \right) + f_p \left( \frac{-\omega}{2\pi h_i} \right) \right] \quad (3)$$

When wheel speed is a uniform random variable over the interval  $[f_1, f_2]$ , the power spectral density becomes:

$$\Phi_m(\omega) = \sum_{i=1}^n \Phi_i(\omega)$$

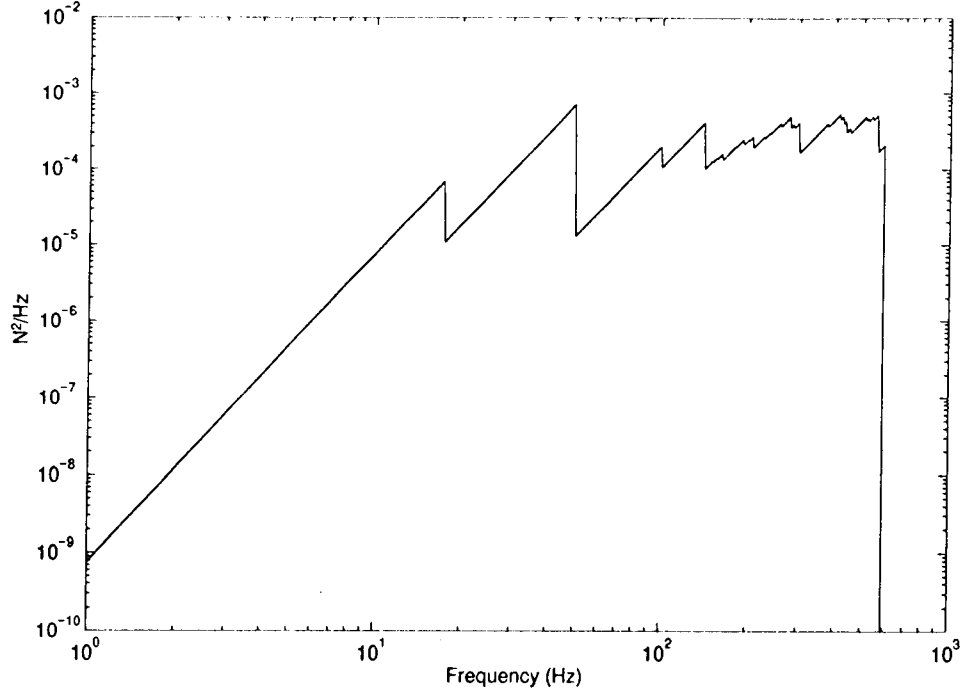


Figure 3: Stochastic reaction wheel axial-force disturbance power spectral density assuming a uniform random variable wheel speed over the interval  $[0, 3000]$  rpm.

$$\Phi_i(\omega) = \begin{cases} \frac{\pi C_i^2}{2(f_2 - f_1)(2\pi h_i)^5} \omega^4 & \text{for } 2\pi h_i f_1 < |\omega| < 2\pi h_i f_2 \\ 0 & \text{otherwise} \end{cases} \quad (4)$$

Figure 3 shows the axial-force PSD for a uniform random variable wheel speed over the interval  $[0, 3000]$  rpm.

### 3 Six-Axis Active Vibration Isolation

The platform on which the vibration source is placed is suspended on six identical active struts in an orthogonal (hexapod) configuration (see Figure 1). Each active strut contains a diaphragm which allows motion only in the axial direction. For this direction, the diaphragm represents a reasonably soft spring. In parallel with this spring is a voice coil actuator. The strut is connected to the structure in series with an axial-force sensor and two axially stiff, cross-blade flexures serving to reduce coupling between struts. The active strut design is described in detail in reference [8]. The stiffness of the diaphragm was chosen such that the vertical mount mode is roughly 10 Hz, small enough to provide sufficient passive vibration isolation above the controller bandwidth. At the same time the diaphragm is stiff enough

to pass reaction wheel attitude control torques and to accommodate gravity sag. Ideally, each strut transmits force only in the axial direction. However, due to imperfect cross-blade flexures, each strut passes non-axial vibrations as well, creating coupling between the struts.

Disturbance isolation must be especially large over the range of 20 to 60 Hz where feedback in the optical control loop is limited and therefore fails to sufficiently reduce the disturbances. In this frequency range, the isolation provided by the strut must be increased by application of feedback from the force sensor to the voice coil in each strut. This feedback is SISO, and each of the six loops is largely decoupled from the other five loops.

Feedback in the active strut changes the logarithmic force transfer function,  $\log |K_F|$ , by  $\Delta \log |K_F|$ . Specifically,  $K_F$  is the ratio of A) the vibration force applied by the strut to the base structure to B) the force applied by the vibration source. The integral of this change along the inverse frequency scale must be zero [9]:

$$\int_0^\infty \Delta \log |K_F(\omega)| d\omega^{-1} = 0 \quad (5)$$

In other words, when the disturbance propagation is reduced over some range, it is increased over a different range. The disturbance propagation needs to be reduced in the range of 10 to 100 Hz. At frequencies lower than 10 Hz, the disturbance propagation will be increased by feedback. However, the active optical loop has large feedback in this range. At high frequency, sufficient disturbance isolation is provided passively, by the softness of the diaphragm of the active strut.

We apply the disturbance isolation control to the base structure having many flexible modes with uncertain frequencies. For this system to be stable, the active-strut mobility function must be positive real. For the disturbance isolation to be large, the modulus of the mobility must be made large. In addition, the real component of the mobility needs to be paid attention to in order to reduce transmission at the frequencies of the lightly-damped structural modes.

Generally, the strut mobility is:

$$Z = Z_o(1 + T_F) \quad (6)$$

where  $Z_o$  is the strut mobility without feedback and  $T_F$  is the force feedback loop transfer function. The mobility phase angle must be within the interval  $-90^\circ$  to  $90^\circ$ . Since  $Z_o$  degenerates at low frequency into the diaphragm mobility whose phase angle is  $90^\circ$ , the phase angle of  $(1 + T_F)$  at low frequency must approach zero. In other words, the force feedback must degenerate into a constant.

An amplifier with high output impedance (*i.e.*, a current driver) drives the voice coil. In this case the back electro-motive force has no effect and the vibration force transmission without feedback (and with amplifier power on) is only that caused by the diaphragm stiffness. Compared to the case of using a voltage driver, this substantially reduces  $|K_F|$  without feedback over the range up to 60 Hz. At high frequency, where the structure mobility increases, the choice of current or voltage drivers makes no difference since the mobility of the voice coil is already much larger than the mobility of the load. As an additional advantage,

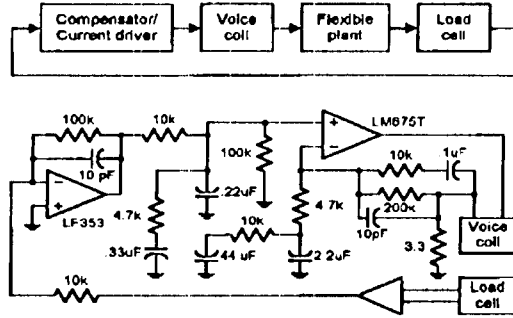


Figure 4: Block diagram of one-direction vibration isolation feedback loop and the related circuit diagram.

using current drivers reduces both the effects of the flexible structure on the feedback loop and the coupling between the loops.

Since no commercial current driver was readily available at a reasonable price, the amplifiers were custom designed around power op-amps. (A warning: power op-amps can self-oscillate with frequencies many times higher than their nominal 0 dB gain frequency when the loads are reactive. To prevent the oscillation, filter capacitors need to be appropriately placed and wire connections need to be short as governed by RF design rules.) Since the actuator inputs and the load cell outputs are all analog, the feedback loop compensators were also implemented as analog active RC-circuits (see Figure 4), resulting in a stand-alone system. Although active isolation modifies the plant for both optical control and attitude control, the plant for each remains passive.

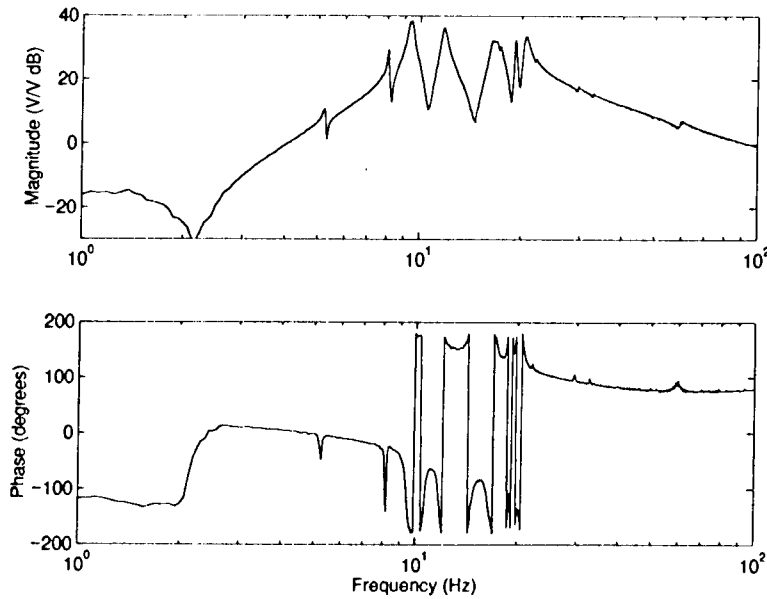


Figure 5: Isolator loop gain for a single strut with all others loops closed.

The Bode diagram for a feedback loop measured with all other five loops closed is shown in Figure 5. All individual loop responses are similar, and the coupling between the individual loops is smaller than -30 dB over the frequency range up to 100 Hz.

## 4 Fringe Tracker Control System

The interferometer requires a number of optical control systems in order to perform a measurement. These consist of coarse starlight acquisition, fine pointing, and pathlength control. While acquisition and pointing control enable measurement of the interference fringe, it is the fringe tracker control system that directly affects the performance quantity, stellar pathlength. Therefore, only the fringe tracker control is described in detail. For more information on the other optical control systems, see references [10, 11].

The fringe tracker control system must equalize the optical paths from the star through each arm of the interferometer to the point where they are combined. This subsystem must provide the required disturbance rejection below 10 Hz, and share responsibility with the isolation system between 10 Hz and 300 Hz. On-orbit, photon statistics associated with dim stellar targets are expected to limit fringe tracker bandwidth to a few hundred Hz. This translates into the following top-level requirements:

- Open-loop bandwidth must be less than 300 Hz.
- Loop gain up to 300 Hz should be maximized.
- Closed-loop system must have gain margins of at least 6 dB and phase margins of at least 30°.

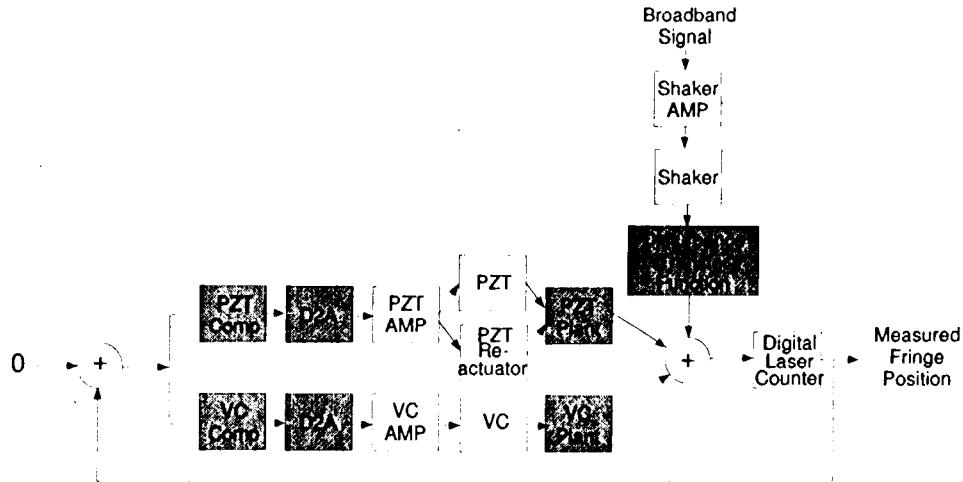


Figure 6: Fringe tracker control system implementation.

Figure 6 shows a block diagram of the control system implementation. The error signal for the system is fringe position. Figure 7 shows the complete optical layout for the testbed



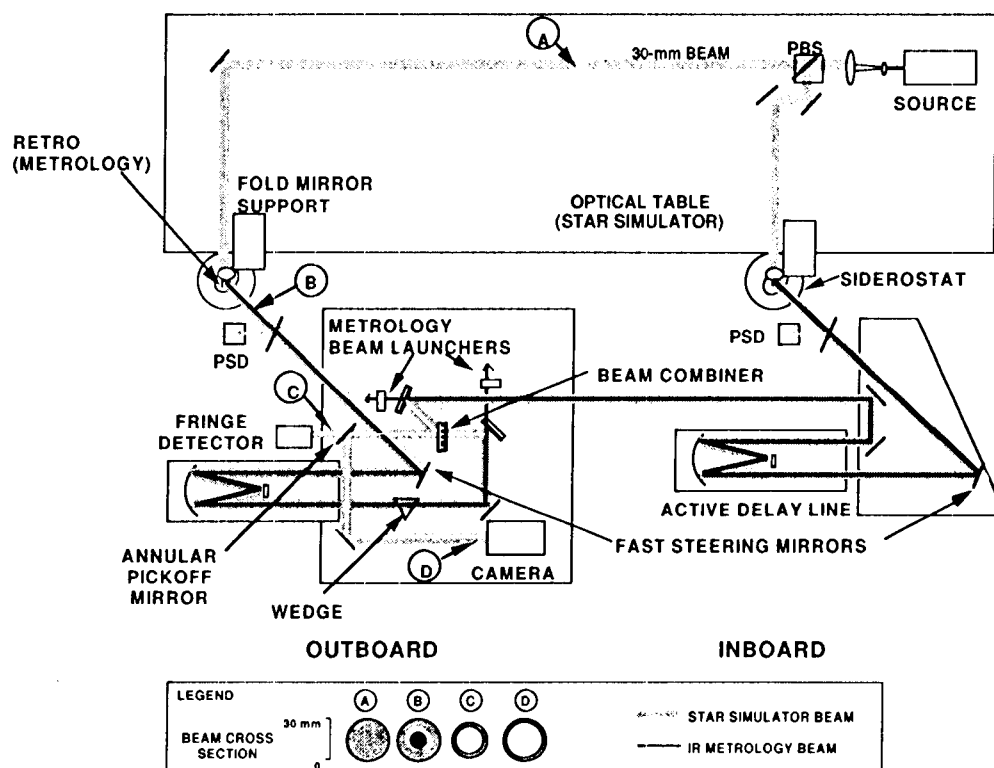
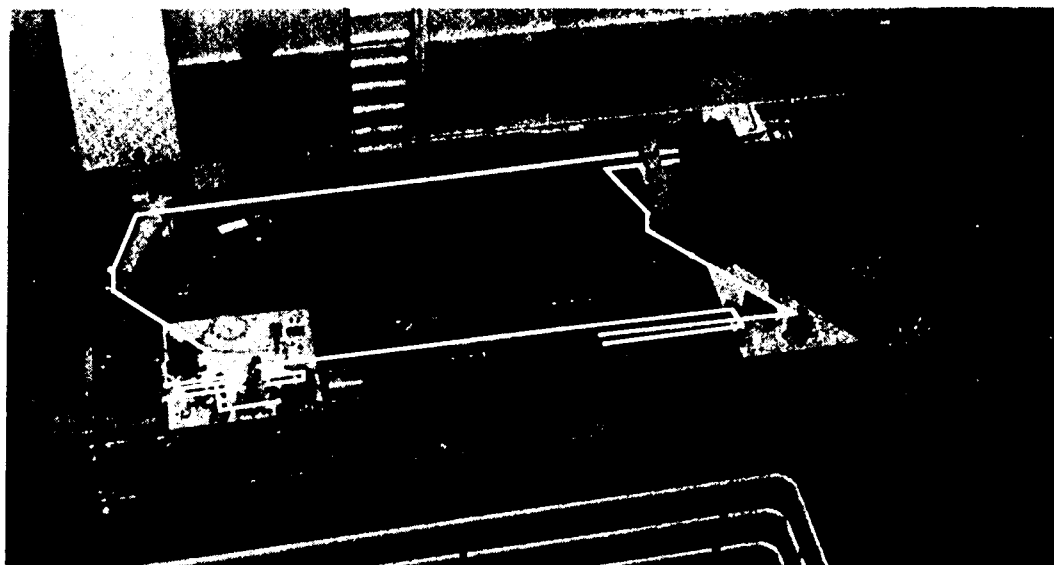


Figure 7: MPI optical layout. Block diagram identifies significant optical components. Both the block diagram and the photo depict the same region. Inset shows beam diameter at different points in the optical path.

and pseudo star. The stellar source, a HeNe 633 nm laser, is located on a passively-isolated, four meter optical table. This beam is split and directed with flat mirrors to the respective testbed collecting apertures. The testbed is suspended from the ceiling with an active pneumatic/electromagnetic suspension system, with suspension modes all below 1 Hz. Starting with each collecting aperture (or siderostat) the stellar light bounces off twelve surfaces in each interferometer arm before entering the fringe detector. These mirrors are attached to one of six independent mounting plates which are kinematically attached to the testbed. Fringe position variation results from disturbances influencing rigid body motion of the structure relative to the pseudo star table, global modes of the structure, mount modes of the plates, flexible modes of the plates and flexible modes of the individual optical mounts.

The active delay line actually consists of three actuators, each of which has a unique stroke and bandwidth. Together, these actuators introduce the commanded optical delay into one interferometer arm with the resolution and bandwidth of the small signal actuator and the dynamic range of the large stroke actuator. The three stages are: a stepper motor for low-frequency (dc), long-travel capability (1 m); an intermediate voice-coil actuator for medium-frequency (dc - 10 Hz), medium-amplitude control (cm); and a reactuated piezoelectric device (PZT) for high-bandwidth (up to kHz), precise actuation ( $\mu\text{m}$ ).

The delay line optical assembly contains a six-inch parabolic primary mirror (with  $f/\#$  of three) and a half-inch flat secondary mirror. Collimated light entering the assembly reflects off of the primary, the secondary, and the primary again, returning collimated and parallel to the input direction but displaced vertically. The delay line is set in a cart that moves on precision rails along the delay line's optical axis. This cart is actuated by the stepper motor, providing very large optical delays used in fringe acquisition. Within the optics cart, the optical assembly is flexured at 1.15 Hz translationally along its optical axis. The eight Bendix flexures holding the optical assembly also provide stiffness in the transverse axes in order to maintain optical alignment. The voice-coil motor actuates in parallel with the assembly flexures, providing the second actuator stage by moving the entire optical assembly. Finally, a PZT moves the secondary mirror within the optical assembly. A reactuator PZT is diametrically mounted to the base of the secondary mirror PZT. Generally, the optics cart stepper motor is fixed during observations. Hence, only the voice-coil and the PZT are significant to the vibration attenuation design.

The fringe tracker control algorithm is implemented digitally on a single 68040 microprocessor. This cpu is one of ten that operate the entire MPI instrument using a VME/Sun host computer architecture. This loop provides commands to the delay line at 8 kHz. The fringe position is measured with a custom digital laser counter board. This board can provide 2.5 nm resolution (8 bits fractional position) for a single pass, 633 nm laser.

This is a two input, one output control problem. The two actuators are configured in parallel. In this configuration, the control design approach maps directly to the assignment of a specific actuator control authority to specific frequency regimes. This is analogous to the approach taken in reference [5].

Since the voice coil moves the significant mass of the entire optical assembly, this plant transfer function couples with structural dynamics. In contrast, the PZT plant shows no sign

of coupling to the structure. This decoupling is achieved by providing both the secondary mirror PZT and the reactuation PZT with the same command, allowing the reaction forces of the two PZTs to cancel.

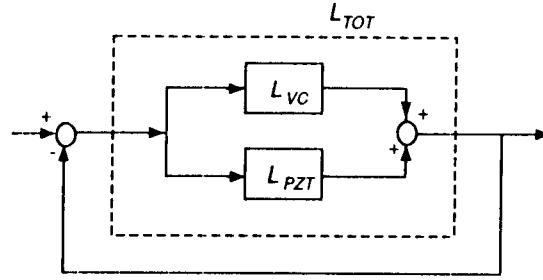


Figure 8: Fringe tracker control system block diagram.

Figure 8 shows the control system block diagram in terms of the PZT, voice coil, and total loop gains:  $L_{PZT}(j\omega)$ ,  $L_{VC}(j\omega)$ , and  $L_{TOT}(j\omega)$ , respectively. The design objective is for  $L_{VC}$  to dominate at low frequency and  $L_{PZT}$  to dominate at high frequency. Closed-loop stability requires that attention be paid not only to the 0 dB crossover ( $f_{co}$ ) of the total loop gain,  $L_{TOT}$ , but also to the relationship between the parallel paths near the “hand-off” frequency,  $f_{ho}$ , defined by:

$$|L_{PZT}(2\pi j f_{ho})| = |L_{VC}(2\pi j f_{ho})| \quad (7)$$

In fact, two functions must be Nyquist stable in order to ensure closed-loop stability:  $L_{TOT}(j\omega)$  and the ratio of  $L_{VC}(j\omega)$  to  $L_{PZT}(j\omega)$  [12]. Figure 9 shows the three loop gains  $L_{PZT}$ ,  $L_{VC}$  and  $L_{TOT}$ , and Figure 10 depicts the ratio of  $L_{VC}$  to  $L_{PZT}$ .

Given the expected disturbance spectra, the PZT actuator dynamic range enforces a lower limit on  $f_{ho}$ . On the other hand, the influence of structural modes in the voice-coil plant transfer function reduces hand-off stability margins as  $f_{ho}$  is increased (see Figure 10). Within these constraints, the hand-off frequency was chosen to be 7 Hz. Classical control design methods were used to frequency-shape the loops for maximum feedback, based on laboratory measurements of the plant transfer functions. The resulting system has an open-loop bandwidth of 300 Hz. Both Figures 9 and 10 demonstrate that the system is conditionally stable with adequate gain and phase margins.

## 5 Performance Prediction

Predicting on-orbit performance solely in hardware would require simultaneous application of the reaction wheel disturbance power spectra for four wheel orientations. This could be accomplished with some difficulty with a six axis force/torque input device. However, the resulting fringe position data would be corrupted with ambient disturbances not traceable to space such as modes associated with the suspension system, pseudo star motion, and atmospheric effects on the laser beams. The effect of these ambient disturbances on the

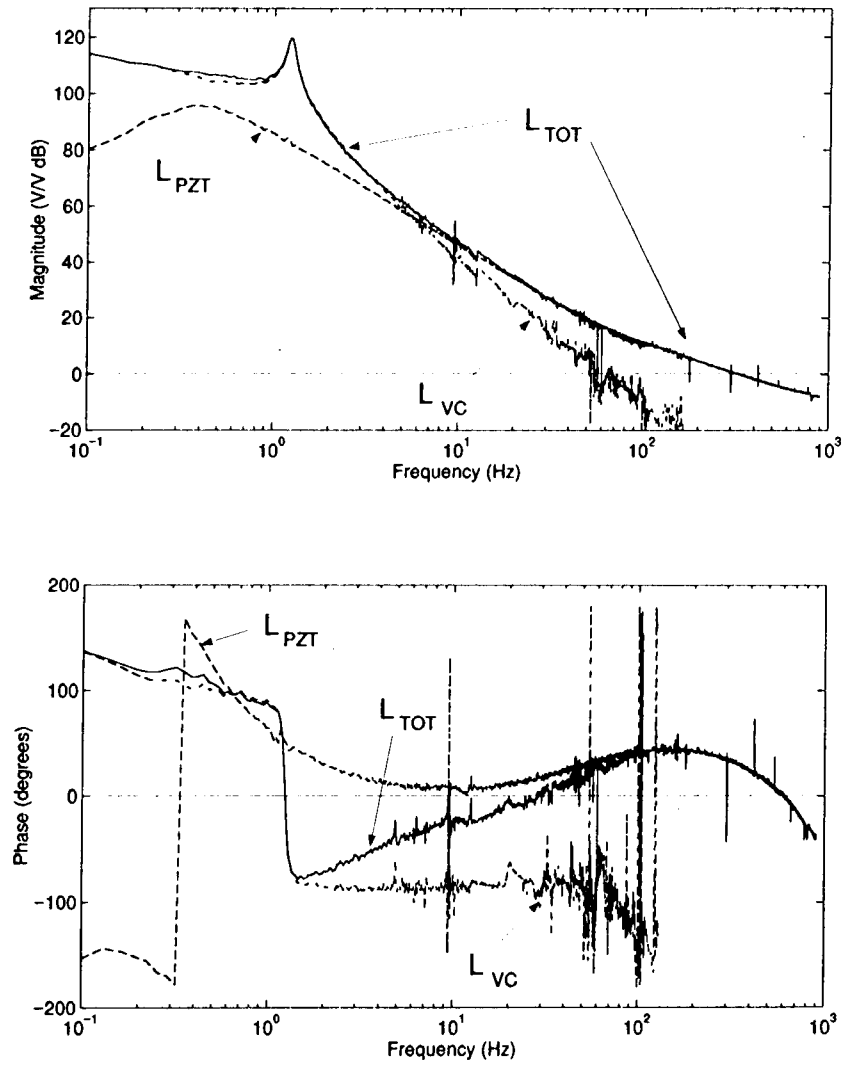


Figure 9: Fringe tracker control system loop gains (magnitude and phase).

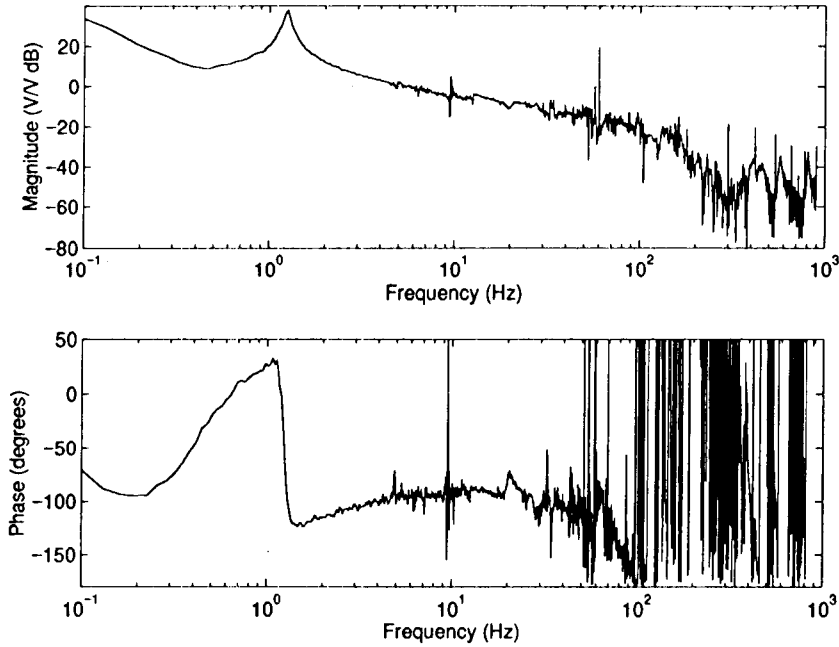


Figure 10: Hand-off frequency stability function (magnitude and phase).

fringe position has been measured to be as high as 10,000 nm (*i.e.*, larger than the 10 nm requirement) [11]. For this reason, a hybrid analytical/experimental performance prediction procedure is used.

This procedure requires measuring broadband transfer functions from the disturbance source attachment location to fringe position output on the testbed, thereby completely characterizing the disturbance transmission paths. The analysis environment enables *on-orbit* prediction by providing three functions: 1) stochastic characterization of reaction wheel disturbances over all conditions, 2) combination of the testbed data with the disturbance model output, and 3) calculation of the resulting fringe position. The disturbance model, as characterized by Eq. 3, generates input force and torque power spectra assuming independent, identically distributed uniform wheel speeds over the interval [0, 3000] rpm. The various wheel orientations are accounted for analytically.

## 5.1 MPI Measurement

The testbed provides the dynamic relationship between the measured disturbance input (*i.e.*, 3 forces and 3 torques) and the optical output (fringe position). Figure 11 shows the disturbance input location and the fringe detector output location used to measure the disturbance transfer functions. Transfer function measurement requires application of pure forces and torques for each input direction.

A 10 N shaker containing a 0.5 kg proof mass applied the force disturbance input in

the testbed x-axis, y-axis, and z-axis directions. An accelerometer mounted to the proof mass was used to derive the input force. Two 10 N shakers, each with a 6 cm moment arm from the center of the disturbance mounting plate, were driven 180° out of phase in order to generate torque input. An HP data analyzer provided the input drive signal for the shakers and calculated the force to fringe position transfer functions, from 2 Hz to 1 kHz. For each direction, this range was broken into three frequency bands in order to create high resolution transfer functions. For the highest frequency range (100 Hz to 1 kHz) a sine sweep was used. Measurement of the other two bands used broadband random excitation. These six measured transfer functions were used to calculate fringe position in response to the modeled reaction wheel disturbances.

## 5.2 Disturbance Analysis

In the analysis environment disturbances of four wheels were modeled, as SIM is expected to carry four reaction wheels for redundancy. These wheels were assumed to be in a pyramidal configuration, *i.e.*, the spin axis of each wheel is normal to a side of a square pyramid. The angle of the pyramid was assumed to be 63°, since this yielded equal torque capacity in all three spacecraft axes. Associated with each wheel orientation is a set of reaction-wheel local coordinates and a transformation from local to global coordinates. Applying this transformation to the disturbance transfer functions yielded transfer functions from each reaction wheel's local disturbance direction to the stellar fringe position. That is, from the six measured transfer functions,  $H_n(j\omega)$ , twenty local-coordinate transfer functions,  $\tilde{H}_{jk}(j\omega)$ , were created (five disturbance directions per wheel,  $j$ , times four wheels,  $k$ ). These twenty transfer functions were then used in the disturbance analysis in order to determine fringe position resulting from each wheel orientation.

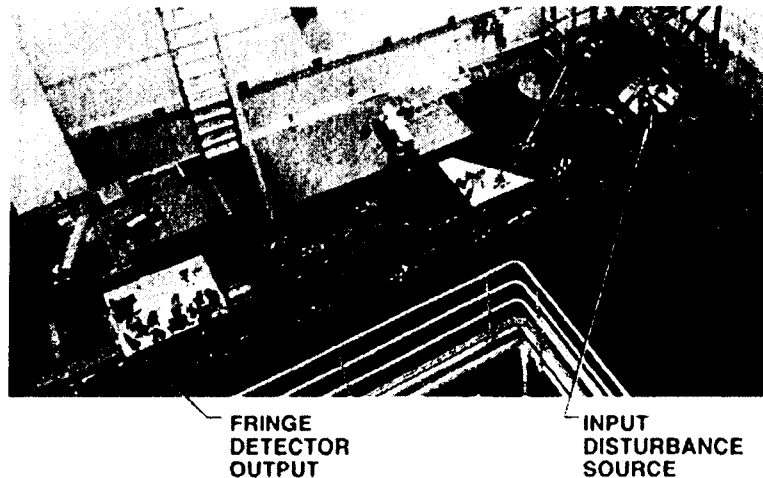


Figure 11: Relation between the disturbance input location and the fringe detector output location on the MPI testbed.

The kernel of the procedure is the calculation of a fringe position standard deviation,  $\sigma_{fp}^k$ , for each wheel orientation,  $k$ . This calculation begins with five reaction wheel disturbance power spectra generated from a uniform wheel speed over  $[0, 3000]$  rpm (an example reaction wheel disturbance PSD is shown in Figure 3). These power spectra,  $\Phi_m^j(\omega)$ , are multiplied by the modulus squared of their corresponding local disturbance transfer functions,  $\tilde{H}_{jk}(j\omega)$ , and summed to yield the fringe position PSD,  $\Phi_{fp}^k(\omega)$ :

$$\Phi_{fp}^k(\omega) = \sum_{j=1}^5 \left| \tilde{H}_{jk}(j\omega) \right|^2 \Phi_m^j(\omega) \quad (8)$$

An example fringe position PSD is shown in Figure 12.

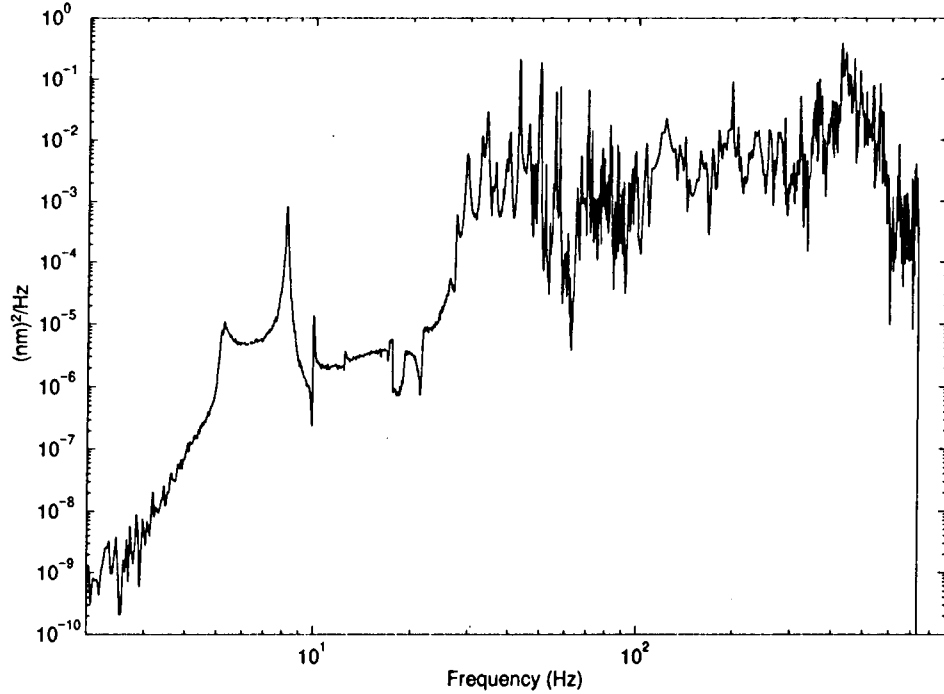


Figure 12: Fringe position power spectral density,  $\Phi_{fp}^k(\omega)$ .

Integration of the fringe position PSD yields the standard deviation,  $\sigma_{fp}^k$  over all wheel speeds for a given wheel orientation:

$$\left[ \sigma_{fp}^k \right]^2 = \frac{1}{\pi} \int_0^\infty \Phi_{fp}^k(\omega) d\omega \quad (9)$$

Assuming that the wheel speeds are stochastically independent, the variance of fringe position resulting from disturbances of all four wheels,  $\sigma_{fp}^2$ , is the sum of the separate variances. In other words,  $\sigma_{fp}^2$  can be interpreted as the result of a covariance analysis where the four wheel speeds are assumed to be independent and uniform over  $[0, 3000]$  rpm.

## 6 Results

Instrument performance was predicted for a number of testbed configurations in order to understand the contribution of each attenuation layer. These configurations are: no control (hard mounted disturbance, no active optics); active optics (hard mounted disturbance, optical control loops operational); and completely active (active isolation of disturbance, optical control loops operational). The six disturbance transfer functions (3 forces and 3 torques) from the disturbance input location to fringe position output, were measured for each of these configurations. Figure 13 shows the x-axis torque disturbance transfer function for the no control configuration and the active optics configuration. These two transfer functions demonstrate the aggressive control authority of the active optics in the low frequency region. Figure 14 compares the no control configuration with the completely active configuration for the x-axis torque input. Comparison of these two plots indicate the broadband nature of the layered architecture in which active optics provides vibration attenuation at low frequencies and active isolation system provides vibration attenuation at high frequencies.

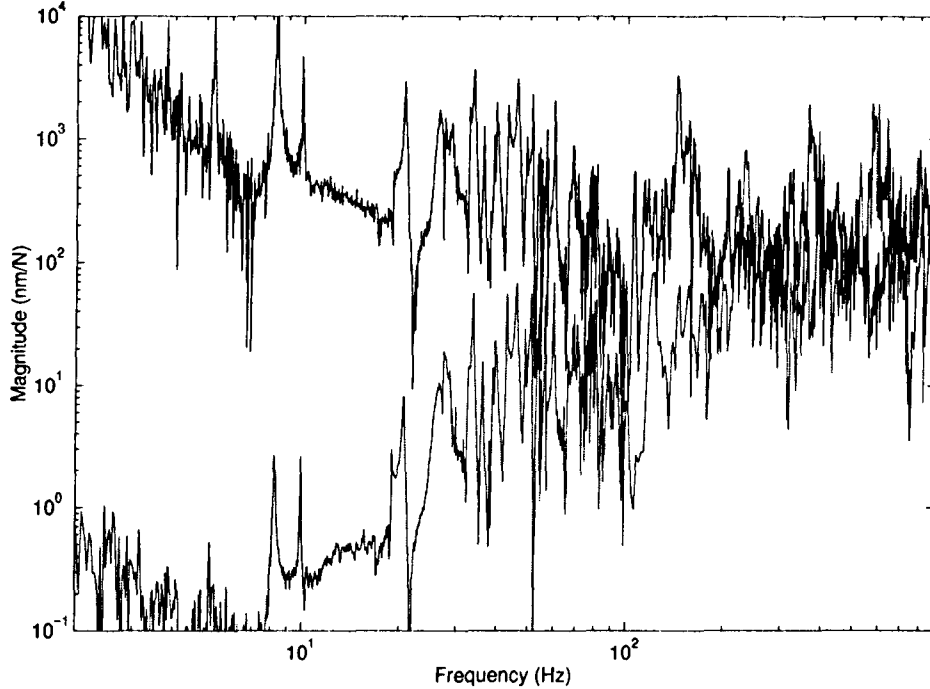


Figure 13: x-axis torque to stellar fringe position with no control (top curve) and with active optics only (bottom curve).

Table 1 summarizes for each configuration the resulting fringe position for each wheel orientation,  $\sigma_{fp}^k$  and for all wheels,  $\sigma_{fp}$ . Note that the required fringe stabilization value of 10 nm is satisfied when both active optics and active isolation are used. This represents the likely operating conditions for the mission during an astrometric observation. More compre-



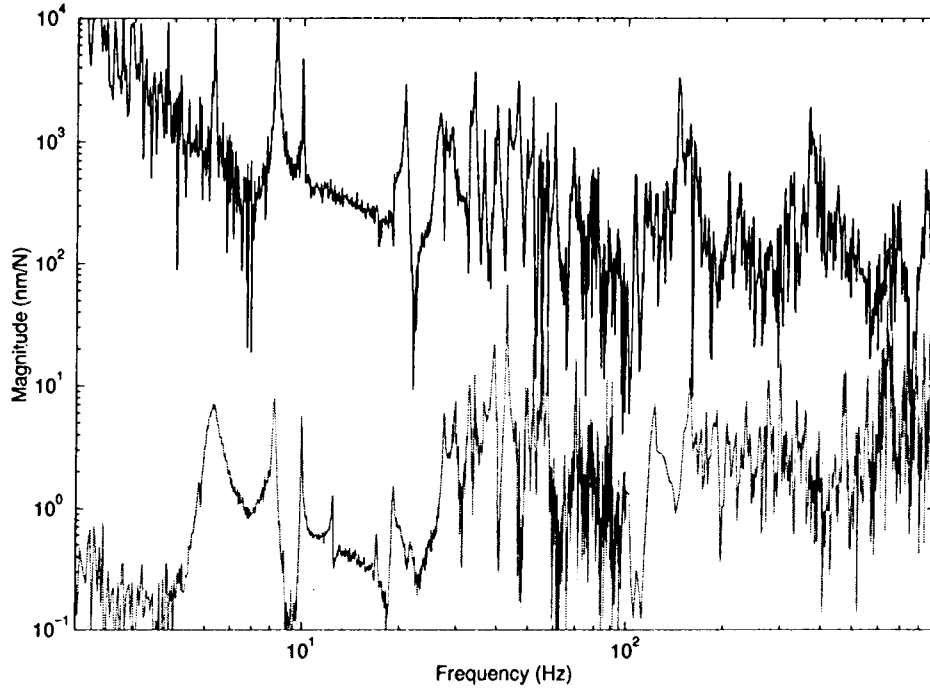


Figure 14: x-axis torque to stellar fringe position with no control (top curve) and with active optics and active isolation (bottom curve).

hensive characterization of instrument performance, using the discrete-frequency disturbance model for each possible wheel speed, is the subject of continuing work.

RWA # ( <i>k</i> -index)	Hard-mounted No Control	Hard-mounted Active Optics	Active Isolation Active Optics
1	398.2	94.2	4.9
2	375.4	93.3	4.9
3	380.5	92.9	5.2
4	311.4	89.5	5.2
All	735.7	185.0	10.1

Table 1: Summary of resultant fringe position,  $\sigma_{fp}$  (given in nm).

A number of modifications could be made to the implemented vibration attenuation strategy in order to provide interferometer performance margin. For example, active and/or passive dampers could be added to the structure to attenuate specific structural modes which have a significant negative impact on system performance. Another strategy would be to reduce the isolation mount modes by perhaps a factor of ten (from 10 Hz to 1 Hz for the vertical mode) thus increasing the passive attenuation at high frequencies by a factor

of one hundred. A more ambitious approach would be to go beyond linear time-invariant control theory and implement discrete-frequency tracking vibration isolation [13]. In this case system performance could be significantly improved by adaptively tracking the moving reaction wheel disturbance harmonics and providing this tracked signal as feedforward to the broadband isolation controllers.

## 7 Conclusions

A vibration attenuation strategy consisting of vibration isolation and optical control for spaceborne interferometers has been proposed and implemented on the Micro-Precision Interferometer testbed. The effectiveness of the vibration attenuation strategy is evaluated by combining a stochastic model of the primary disturbance source, spinning reaction wheels, with measurements from the testbed. This allows prediction of interferometer performance in the presence of on-orbit disturbances, hence evaluating the effectiveness of vibration attenuation. Successive application of A) active optics only and B) active isolation and active optics together validate the synergy of the low-frequency attenuation of active optics and the high-frequency attenuation of active isolation into a broadband attenuation strategy. With this broadband strategy in place, the positional stability requirement of 10 nm is achieved.

## 8 Acknowledgments

The research described was performed at the Jet Propulsion Laboratory of the California Institute of Technology, under contract with the National Aeronautics and Space Administration. The authors thank John Carson for his extensive contribution to the testbed measurements; Noble Nerheim, Peter Gluck, John Spanos, John O'Brien, Rob Calvet, Brad Hines, and Stuart Shaklan for their efforts; and the leaders of the Interferometer Technology Program, Bob Laskin, Jeffrey Yu, and Ben Parvin for their technical and financial support.

## References

- [1] M. Shao and D. M. Wolff, "Orbiting stellar interferometer," in *Spaceborne Interferometry II* (R. D. Reasenberg, ed.), vol. 2447 of *Proc. SPIE*, (Orlando, FL), pp. 228-239, Apr. 1995.
- [2] M. Shao, M. M. Colavita, B. E. Hines, D. H. Staelin, D. J. Hutter, K. J. Johnston, D. Mozurkewich, R. S. Simon, J. L. Hersey, J. A. Hughes, and G. H. Kaplan, "Mark III stellar interferometer," *Journal of Astronomy and Astrophysics*, vol. 193, pp. 357-371, 1988.
- [3] M. M. Colavita, M. Shao, B. E. Hines, J. K. Wallace, Y. Gursel, C. A. Beichman, X. P. Pan, T. Nakajima, and S. R. Kulkarni, "Palomar interferometer testbed," in *Amplitude and Intensity Spatial Interferometry II* (J. B. Breckinridge, ed.), vol. 2200 of *Proc. SPIE*, (Kona, HI), pp. 89-97, Mar. 1994.
- [4] R. A. Laskin and A. M. San Martin, "Control/structure system design of a spaceborne optical interferometer," in *Proc. AAS/AIAA Astrodynamics Specialist Conference*, (Stowe, VT), Aug. 1989.

- [5] J. T. Spanos, Z. Rahman, C.-C. Chu, and J. F. O'Brien, "Control structure interaction in long baseline space interferometers," in *Proc. 12<sup>th</sup> IFAC Symposium on Automatic Control in Aerospace*, (Ottoobrunn, Germany), Sept. 1992.
- [6] M. D. Hasha, "Reaction wheel mechanical noise variations," Engineering Memorandum SSS 218, LMSC, June 1986.
- [7] A. Papoulis, *Probability, Random Variables, and Stochastic Processes*. New York: McGraw-Hill, 3<sup>rd</sup> ed., 1991.
- [8] J. T. Spanos, Z. Rahman, and G. H. Blackwood, "A soft 6-axis active vibration isolator," in *Proc. American Control Conference*, (Seattle, WA), June 1995.
- [9] B. J. Lurie, "Integral relations for disturbance isolation," *AIAA Journal of Guidance, Control, and Dynamics*, vol. 20, May-June 1997.
- [10] J. F. O'Brien and G. W. Neat, "Micro-precision interferometer: Pointing control system," in *Proc. 4<sup>th</sup> Conference on Control Applications*, (Albany, NY), Sept. 1995.
- [11] G. W. Neat, A. Abramovici, J. W. Melody, R. J. Calvet, N. M. Nerheim, and J. F. O'Brien, "Control technology readiness for spaceborne optical interferometer missions," in *Proc. Space Microdynamics and Accurate Control Symposium*, (Toulouse, France), May 1997.
- [12] B. J. Lurie, *Feedback Maximization*. Artech House, Inc., 1987.
- [13] J. T. Spanos and Z. Rahman, "Narrow-band control experiments in active vibration isolation," in *Vibration Monitoring and Control*, vol. 2264 of *Proc. SPIE*, (San Diego, CA), July 1994.